JOURNAL OF PROPULSION AND POWER
Vol. 21, No. 2, March–April 2005

Role of Wall Shape on the Transition in Axisymmetric Dual-Bell Nozzles

Francesco Nasuti,* Marcello Onofri,† and Emanuele Martelli‡
University of Rome "La Sapienza," Rome 00184, Italy

Dual-bell nozzles represent a possible solution to improve the performance of large liquid rocket engines for launcher first stages. The present paper studies the role of the second bell shape on the side loads that can occur during the transition between the two main operating modes of the nozzle. In particular, the design of the second bell profile is critically discussed on the basis of results obtained from suitable test cases. The analysis of performance and behavior during the transition is carried out by a validated turbulent Navier–Stokes solver. Geometries were generated by the method of characteristics. Results show that slightly different geometries designed by the method of characteristics yield modest performance changes but severe differences in behavior during the transition phase.

Nomenclature

A	=	area
A, B, C	=	specific locations along the nozzle profile
a	=	speed of sound
C_F	=	thrust coefficient
l	=	length
PR	=	nozzle pressure ratio, $= p_c/p_a$
p	=	pressure
Re	=	nozzle Reynolds number, $= \rho_c a_c r_t/\mu_c$
r	=	radius (distance from the symmetry axis)
T	=	temperature
t	=	time
x	=	distance along the symmetry axis
α, β	=	coefficients
γ	=	ratio of specific heats
ϵ	=	area ratio (A/A_t)
μ	=	viscosity
ρ	=	density

Subscripts

a	=	ambient
b	=	base
c	=	chamber
e	=	extension
i	=	inflection point region
id	=	ideal
s	=	separation point
t	=	throat
tr	=	transition

Superscript

$'$	=	nondimensional value

Introduction

LAUNCHER first-stage engines operate in a varying pressure environment, from sea-level to nearly vacuum conditions. For this reason the conventional bell nozzles, which feature a single adaptation altitude, cannot yield the maximum performance along the whole trajectory. Although the ideal propulsion device would be an engine with adapted nozzle during its whole operating phase, a nozzle featuring a high adaptation altitude would be a good solution to provide high engine performance, as most of the operation of the main-stage engines takes place at high altitudes (low pressures). Unfortunately this approach cannot be accepted because of the generation of heavy side loads that take place during the overexpanded phase at sea level. In fact, the expansion ratio of present bell nozzles is strongly limited by this phenomenon. To improve the average thrust coefficient of main engine nozzles and, consequently, the launcher performance and the relative payload mass, different nozzle concepts have been studied, aiming at closing the gap between present and ideal engines.[1,2]

Among new nozzle concepts, the dual-bell nozzle[3–6] is one of the most promising choices. The idea of the dual-bell design is to have a nozzle capable of operating at adapted conditions at two different altitudes without the aid of moving parts that could compromise the engine reliability. Indeed, the double adaptation altitude is obtained by means of a geometrical discontinuity of the nozzle profile, which yields two different operating modes, depending on the ambient conditions met during the flight. In particular, the divergent section features two bells with different exit area (base and extension), connected at the inflection point A (Fig. 1). At low altitude (first operating mode, OM1) the flow is attached throughout the first bell and separated downstream the inflection point (Fig. 2a). In this latter case a controlled separation is achieved,[3,6] guaranteeing lower side loads than in overexpanded conventional bell nozzles when flow separation occurs. The reason is that the separation point remains placed about a precise location, the inflection point, for a wide range of nozzle pressure ratios [pressure ratio (PR)—chamber pressure divided by ambient pressure]. This is caused by the strong pressure gradient at the inflection point, so that any chamber and ambient pressure fluctuation displaces the separation point only slightly. As a consequence, lower side loads are generated compared with conventional nozzles, which, on the contrary, show a smaller pressure gradient and therefore a larger displacement of the separation point.[5,7] On the other hand, at high altitude (second operating mode, OM2) the nozzle operates with attached flow in the whole divergent section (Fig. 2b). The limitation of nozzle expansion ratio caused by sea-level operation can therefore be circumvented, and, consequently, higher vacuum specific impulse be obtained, compared with classical bell nozzles that feature a single adaptation altitude. A further possible benefit of dual-bell nozzles comes from the possible choice of low-cost heat-resistant materials for the nozzle extension.[8]

Although recent studies have provided more insight into the advantages and drawbacks of dual-bell nozzles, before they become a practical alternative to conventional nozzles further investigations are necessary, including both numerical and experimental analyses.

Presented as Paper 2003-4911 at the AIAA/ASME/SAE/ASEE 39th Joint Propulsion Conference and Exhibit, Huntsville, AL, 20–23 July 2003; received 17 November 2003; revision received 25 May 2004; accepted for publication 20 May 2004.

*Ph.D. Assistant Professor. Senior Member AIAA.
†Professor. Senior Member AIAA.
‡Ph.D. Student.

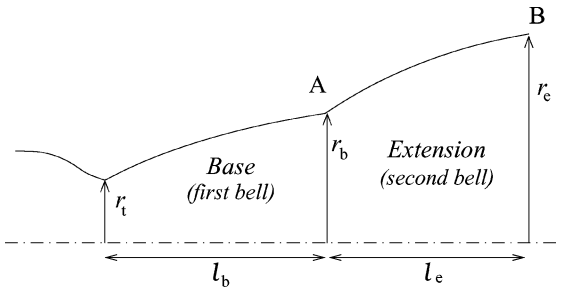

Fig. 1 Schematic of a dual-bell nozzle.

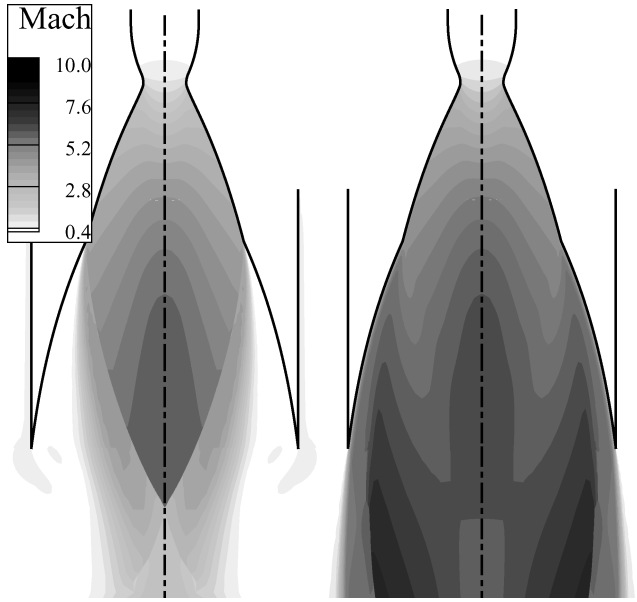

a) OM1 **b) OM2**

Fig. 2 Two main operating modes of a dual-bell nozzle.

In particular, improvements of the nozzle geometry design techniques demand that the flow behavior during the transition between the two operating modes be better understood.

Aim of the present paper is to numerically investigate some design features of dual-bell nozzles. To this goal a suitable design tool for dual-bell nozzle profiles has been developed and subsequently used to obtain three different shapes of the dual-bell nozzle extension. Then the flow behavior in these nozzles has been analyzed by a validated turbulent Navier–Stokes solver, with particular attention devoted to comparing performance and to investigating the transition features between the two operating modes.

Design Goals

Before examining the design approach, it is useful to summarize the main goals of the dual-bell nozzle design. The first goal is to develop a nozzle shape capable of delivering two distinct operating modes (OM1 and OM2), each featuring a different adaptation altitude, and a rapid transition from OM1 to OM2. With reference to the latter statement, note that, because of possible pressure fluctuations, transition might not be axisymmetric, and thus the maximum side loads are reasonably expected during the transition phase,[6] which is therefore desired to be as short as possible.[5] These requirements limit the choice of possible profiles to those exhibiting no stable position for the separation line along the second bell. Indeed, if the separation line were steadily located along the wall of the second bell, long-lasting side loads could occur, like in case of highly overexpanded conventional bell nozzles.

The second goal of dual-bell nozzle design is to obtain the maximum nozzle efficiency both in OM1 and OM2 within the constraint given by the first goal. To this end, it is useful to compare the dual-bell nozzle performance with that of two reference nozzles: 1) a bell nozzle (BN1) with area ratio $\epsilon = \epsilon_b = A_b/A_t$, equal to the area ratio of the dual-bell nozzle base; 2) a bell nozzle (BN2) with area ratio $\epsilon = \epsilon_e = A_e/A_t$, equal to the area ratio of the dual-bell nozzle extension. In the case of OM1, the performance will be slightly lower than that delivered by BN1. This is because during OM1 the flow is separated at the inflection point, and, because of the recirculation that takes place along the second bell, a pressure lower than the ambient pressure acts on the extension wall, thus generating an aspiration drag.[6] As a consequence, OM1 requires maximum performance of base nozzle and minimum aspiration drag. In the case of OM2, featuring attached flow along the whole nozzle wall, the best performance would be provided by a single-bell nozzle designed for the same expansion ratio as the dual-bell nozzle (i.e., BN2). However, because of the inflection point, during OM2 the dual-bell nozzle displays a performance lower than BN2. Of course, the dual-bell nozzle concept is of interest only if it provides during OM2 a significant improvement of performance compared to BN1.

To meet these goals, three families of profiles of the second bell (extension) have been considered[3,6]: 1) profiles showing increasing wall pressure towards the exit during OM2 (positive pressure gradient), 2) profiles showing constant wall pressure (zero pressure gradient), and finally 3) profiles showing decreasing wall pressure (negative pressure gradient). It has been stressed[6,9] that second bell profiles with negative pressure gradient would behave like conventional nozzles, with stable positions of the separation location along the whole profile, and can thus be excluded as a design choice for dual-bell nozzles. On the contrary, constant pressure gradient and positive pressure gradient profiles would lead to indifferently stable and unstable position of the separation location, respectively. In this study, the analysis of the stability of the separation line is carried out, without losing generality, by studying the behavior of the corresponding separation point in the axisymmetric case.

In summary, if the design of the first bell can be carried out as for conventional nozzles, with the constraint that the flow never separates, different requirements must be met when designing the second bell profile, namely, that of providing the maximum performance in OM2, the minimum aspiration drag during OM1, and the shortest transient.

Method of Design

The nozzle design process can be divided in two parts: the first addresses the design of the base and the second the design of the extension. For both parts a design tool based on the method of characteristics has been developed by the authors and implemented in the present study.

Base

As already pointed out, the critical aspects of dual-bell nozzle design are focused on the nozzle operation during transition, which is mainly affected by the second bell shape. The dual-bell nozzle base can therefore be designed using the classical bell nozzle approach, with geometries featuring either a truncated ideal contour,[10] or an optimum thrust contour,[11] or a parabolic contour.[12] In particular, a single truncated ideal contour is chosen in the present study, whose properties are selected according to the subscale cold-flow dual-bell nozzle presented in Ref. 6. The present base nozzle profile features area ratio $\epsilon_b = 16$, length $l'_b = 7.4$ (lengths are nondimensionalized with respect to the throat radius, $r_t = 10$ mm), and is designed for a cold gas with $\gamma = 1.4$.

Extension

The design approach of the second bell (dual-bell nozzle extension) is different than the first bell as the goal is no longer solely that of maximum performance, but also of a safe transition. As just mentioned, to avoid a stable separation location along the second bell a constraint on wall pressure gradient during OM2 must be satisfied: it has to be nonnegative. Therefore, the geometry of the extension is designed by a method-of-characteristics (MOC) calculation of a profile with assigned wall pressure behavior during OM2, satisfying the preceding constraint.

Concerning the method of design, it is interesting to stress that, to provide a description of the profile with sufficient resolution, MOC needs an impractically large number of points on the starting line (i.e., the first wave of the expansion fan). As a consequence the following procedure has been considered for assigned values of ϵ_b, ϵ_e, l'_e (see Fig. 1), and wall pressure behavior (constant, linearly increasing with assigned gradient, . . .):

1) A tentative pressure value downstream the inflection point A (Fig. 1) is selected and the geometry generated by MOC.

2) If the resulting profile does not pass through the assigned point B (Fig. 1), the pressure value downstream of the point A in step 1) is iteratively changed until the profile passes through point B (within an assigned tolerance).

3) Once MOC profile has been generated, the second derivative is computed numerically and smoothed by polynomial best fit: a profile described by a polynomial function is thus obtained.

The preceding design procedure based on the smoothing of the second derivative of the MOC-generated profile was introduced as an improvement on the basic approach of smoothing by polynomial fit of the MOC-generated profile. Indeed, naively using the latter approach can lead to some drawbacks, as discussed later in the paper.

Three different profiles of the extension are discussed in the present paper, each possessing an expansion ratio $\epsilon_e = 38.7$ and extension length $l'_e = 9.6$ (Fig. 1):

1) Constant pressure profile (COP) is the first one, where two profiles are considered, one obtained by a cubic polynomial fit of MOC output, the other by the present method of design (smoothing on the second derivative of MOC output).

2) Linearly increasing pressure profile (LIP) is obtained by the present method of design.

3) Parabolically increasing pressure profile (PIP) is obtained by the present method of design.

Method of Analysis

The analysis of the behavior of the different profiles of the dual-bell nozzle extension is carried out by a validated solver of Reynolds-averaged Navier–Stokes equations, which are integrated by an explicit second-order time-and-space-accurate scheme. This numerical approach, whose main feature is to handle shock discontinuities by a fitting technique,[13,14] has already been used for dual-bell analysis in Refs. 9, 15, and 16, and is particularly suited to compute flow transients. Turbulence is computed by a modified version[17] of the Spalart–Allmaras[18] one-equation model.

Comparison of Different Extension Shapes

The effect of the three extension profiles on the behavior of dual-bell nozzles during transition is analyzed by comparing the relative flowfields, using both steady-state and time-accurate computations. As already mentioned, the profile shape is identified by the wall pressure behavior along the extension in OM2, and the different profiles are named COP, LIP, and PIP, according to the preceding definitions. All of the steady-state simulations have been carried out assuming nitrogen as the working gas, $p_a = 57.14$ kPa, $T_c = 300$ K, and varying chamber pressure p_c to obtain different pressure ratios ($PR = p_c/p_a$). Molecular viscosity is evaluated according to Sutherland's law. Results are nondimensionalized with respect to chamber pressure and throat radius. All of the computations reported in the following have been carried out with similar grids showing the same number of cells (14,240) and clustering law. A discussion on the role of grid resolution on the quality of the solution has been presented in Ref. 9. Based on that discussion, a single resolution level is considered here to compare the role of different extension shapes on the overall flow behavior.

Constant Pressure Extension

The constant pressure profile is obtained by searching for a pressure value that provides a geometry of the extension wall passing through both A and B of Fig. 1. A single solution exists for this problem, which in the present case is the nondimensional constant pressure value $p' = 0.0026$, for the assigned values of $\epsilon_b = 16$, $\epsilon_e = 38.7$, and $l'_e = 9.6$. Note that the reference values for p' and l'_e are chamber pressure ($p_c = 4000$ kPa) and throat radius ($r_t = 10$ mm), respectively.

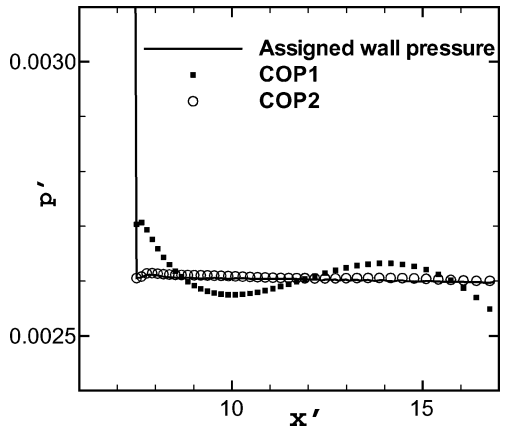

Fig. 3 Comparison among the wall pressure profiles computed for COP1 and COP2 and the assigned wall pressure value.

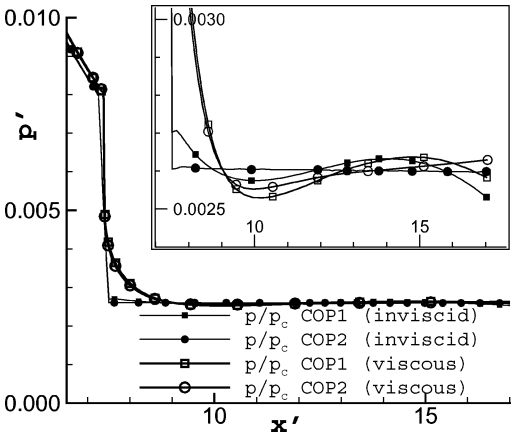

Fig. 4 Comparison of wall pressure along the extension for COP1 and COP2 profiles obtained by inviscid and viscous computations. Wall pressure variations are enhanced in the insert where the same curves are shown on a different pressure scale.

Once the MOC profile is generated, the smooth profile is obtained following two approaches: in the first case (COP1) a polynomial profile is obtained by best fit of the profile generated by MOC; in the second case (COP2) the smoothing is performed by polynomial best fit of the second derivative. The results obtained by both approaches considering third-order polynomials are displayed in Fig. 3. The comparison of wall pressure along the extension shows a wavy behavior in case of COP1: although pressure oscillations feature small amplitude, they yield a change of sign of the pressure gradient. Thus, the COP1 nozzle provides a good approximation of MOC profile, but the inviscid computation of OM2 shows that pressure is no longer constant and displays a sequence of positive and negative gradients. On the contrary the inviscid computation of OM2 for COP2 nozzle shows the expected constant wall pressure along the extension (Fig. 3).

The COP1 and COP2 extensions, as well as the dual-bell nozzle base, are designed using inviscid approaches; therefore, it has to be verified that the desired flow behavior is substantially preserved when viscous and turbulent effects are taken into account. Indeed, viscous effects yield a slight change on wall pressure behavior (Fig. 4). It is interesting to note (see also Fig. 5) that COP2 extension shows a slightly positive value of pressure gradient, whereas for COP1 extension the viscosity enhances the oscillating wall pressure behavior found in the inviscid case. In particular, a negative wall pressure gradient takes place in the last fourth of the second bell.

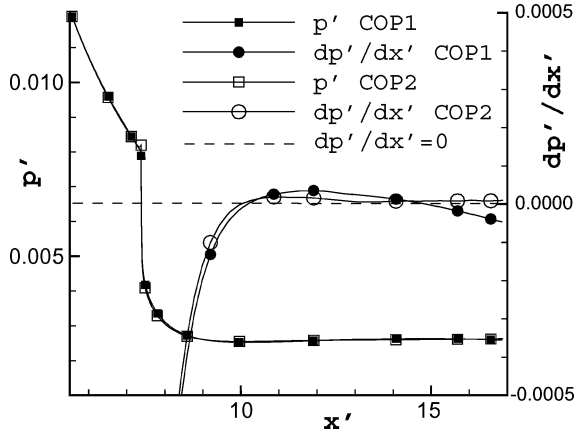

Fig. 5 COP1 and COP2 nozzle wall pressure and wall pressure gradient during OM2.

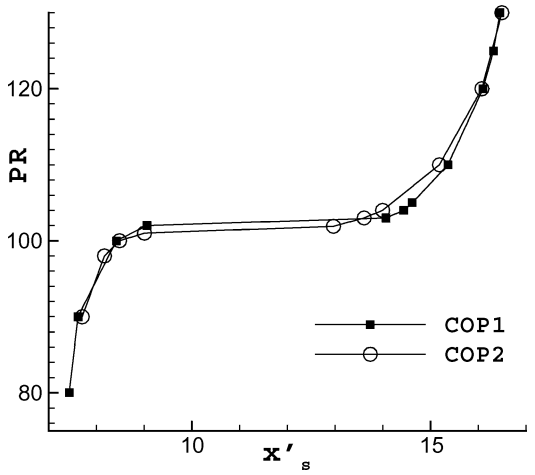

Fig. 6 Position of the separation point for varying *PR* computed by a sequence of steady-state solutions for COP1 and COP2.

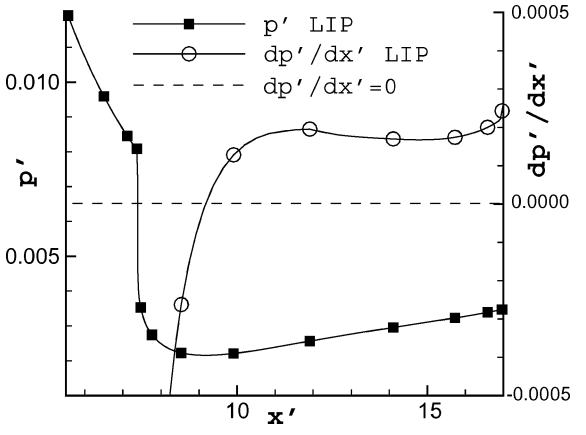

Fig. 7 LIP nozzle wall pressure and wall pressure gradient during OM2.

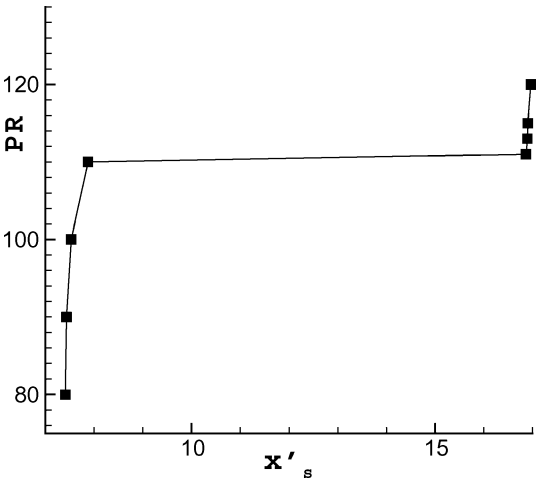

Fig. 8 Position of the separation point for varying *PR* by a sequence of steady-state solutions for LIP nozzle.

The wall pressure behavior in OM2 explains the transition behavior of the position of the separation point computed by a sequence of steady-state computations, each carried out at a different pressure ratio, and displayed in Fig. 6. The sequence of steady-state computations is carried out by starting each computation from the solution at a certain *PR* and changing the chamber pressure value while preserving the same value of ambient pressure (thus changing *PR*). As already noticed in Ref. 9, there are two different regions (at the inflection point and at the nozzle end) where a stable position of the separation point can exist for COP1 extension. These are the regions where the pressure gradient is negative (Fig. 5). A transition across the region of positive gradient is, on the other hand, noticed, which forbids a steady position of the separation point. However, in the case of COP2, where at the nozzle end no regions exist with negative pressure gradient, the solutions show that the separation point finds stable locations close to those obtained for COP1. This behavior indicates that when the pressure gradient assumes values very close to zero a stable location for the separation point is still possible. Indeed, Fig. 5 shows that for COP2 profile $\mathrm{d}p'/\mathrm{d}x' \simeq 0$ when $x' \gtrsim 13$, and stable locations for the separation point are shown for $x' \gtrsim 13$ in Fig. 6.

Linearly Increasing Pressure Extension

Unlike the COP nozzle, where only one MOC profile can be obtained for assigned ϵ_b, ϵ_e, and l'_e, a family of MOC profiles for the extension can be obtained if a linearly increasing pressure behavior is assumed. Indeed, two independent parameters p'_A and $\alpha = (p'_B - p'_A)/l'_e$ define the pressure law:

$$p' = p'_A + \alpha(x' - x'_A) \tag{1}$$

Therefore each profile of the family can be identified by an assigned value of the constant gradient α, whereas the value of p'_A is computed so as to satisfy the constraints on ϵ_b, ϵ_e, and l'_e. Here a single LIP nozzle is considered, featuring a nondimensional gradient $\alpha = 0.00016$. The resulting behavior of pressure and pressure gradient computed by a turbulent simulation during OM2 are displayed in Fig. 7.

The sequence of steady-state solutions from $PR = 80$ to 120 shows in this case that transition takes place at *PR* higher than in case of COP nozzle (compare Figs. 6 and 8). This is explained by the lower minimum pressure value reached in this case just downstream of the inflection point A in OM2 (compare Figs. 5 and 7). However, because of the higher positive gradient (nearly 10 times higher than the maximum value in COP1 nozzle) along the whole extension, a sudden transition takes place, and when the separation point leaves the inflection point region it can still find a new stable location at the nozzle end like in the case of COP nozzle, but only in a very narrow region about the nozzle lip.

Parabolically Increasing Pressure Extension

A further possible degree of freedom is introduced when considering a parabolically increasing wall pressure profile. Here only a family of parabolas starting with pressure gradient equal to zero at the inflection point A is considered. In this case,

$$p' = p'_A + \beta(x' - x'_A)^2 \tag{2}$$

For assigned ϵ_b, ϵ_e, and l'_e, a family of MOC profiles of the extension can be obtained, one for each value of β, where the value of p'_A is computed to satisfy the constraints. Here a PIP nozzle is considered featuring a nondimensional parameter $\beta = 2.6 \times 10^{-5}$. The resulting

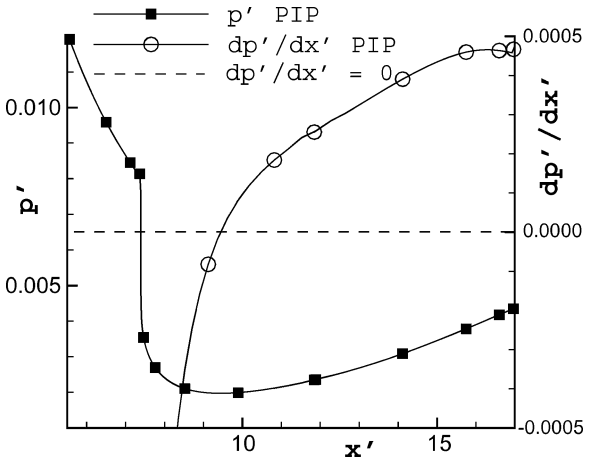

Fig. 9 PIP wall nozzle pressure and wall pressure gradient during OM2.

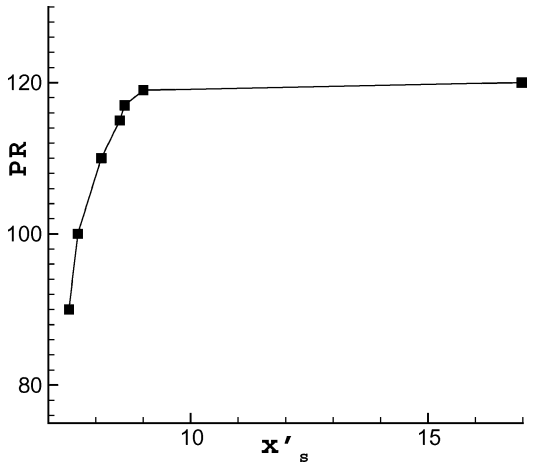

Fig. 10 Position of the separation point for varying *PR* by a sequence of steady-state solutions for PIP nozzle.

behaviors of wall pressure and pressure gradient computed by a turbulent simulation during OM2 are displayed in Fig. 9. The wall pressure increases along the extension reaching a maximum gradient at the nozzle end, with a value nearly equal to two times the constant gradient of LIP nozzle.

The sequence of steady-state solutions from $PR = 90$ to 120 shows in this case that transition takes place at *PR* higher than in case of both COP and LIP nozzles (Fig. 10). The behavior is explained by an even lower minimum pressure value reached just downstream of the inflection point *A*. The present PIP nozzle, because of the increasing pressure gradient toward the nozzle end, does not show the clustering of solutions typical of COP also occurring in the case of LIP.

Performance Comparison

The performance of the three nozzles just illustrated is compared in terms of thrust coefficient and transition behavior. Figure 11 compares the three different extension shapes, where it can be seen that although nozzle profiles are quite similar, the turning at the inflection point A increases from COP to LIP to PIP nozzles, yielding an increasingly stronger expansion fan. Of course, the larger the turning in A, the stronger the overturning from A to B necessary to yield a profile ending in B.

These slightly different extension shapes yield nonnegligible consequences on the dual-bell nozzle efficiency. In particular, the vacuum thrust coefficient is compared for the three different shapes, with the ideal value computed for $\epsilon = 38.7$. In Table 1 the values of C_F for the ideal, COP, LIP, and PIP nozzles are reported on the second column, along with the value obtained in vacuum by a nozzle

Table 1 Comparison of vacuum thrust coefficient for the three different dual-bell nozzles

Nozzle	C_F	$C_F/C_{F,\mathrm{id}}$	wrt COP	wrt base[a]
Ideal	1.720	100.0%	——	——
COP	1.676	97.4%	0.00%	+1.88%
LIP	1.672	97.2%	−0.24%	+1.64%
PIP	1.670	97.1%	−0.36%	+1.52%
Base[a]	1.645	95.6%	−1.85%	+0.00%

[a]Indicates a nozzle made only of the dual-bell nozzle base.

Table 2 Comparison of transition time and pressure ratio

Nozzle	$t'_{\mathrm{tr},1}$	$t'_{\mathrm{tr},2}$	t'_{tr}	PR_{tr}
COP	0.87	0.73	1.60	1.02
LIP	0.93	0.60	1.53	1.10
PIP	1.05	0.56	1.61	1.20

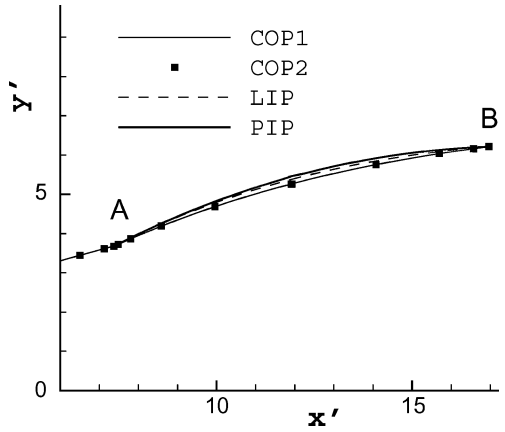

Fig. 11 Comparison of the extension shapes of COP, LIP, and PIP nozzles.

identical to the dual-bell nozzle base. The third column shows the nozzle efficiency evaluated as the ratio of vacuum C_F compared to the ideal value. The fourth column shows the reduction of vacuum C_F with respect to COP nozzle; the fifth column shows the increase of vacuum C_F caused by the extension with respect to the dual-bell nozzle base. The results shown in Table 1 indicate that passing from COP to PIP the overall efficiency reduces by a factor of 0.36%, which cannot be considered negligible if compared to the overall gain in C_F yielded by the second bell (1.52 to 1.88%).

Nevertheless, with regard to the possible reduction of the transition time between the two operating modes, time-accurate simulations show that an important reduction can be achieved by using extension shapes featuring positive values of pressure gradient. In particular, in the present time-accurate simulations chamber pressure is doubled in $t_c = 1.0$ ms, for a constant $p_a = 14.29$ kPa, and *PR* increasing linearly from 90 to 180. Note that the choice of a lower value of p_a with respect to steady-state computations has been made to shorten computational time. Indeed, a lower Reynolds number at the same *PR* and thus a coarser grid in the boundary layer allows for a larger time step. Nondimensionalization of variables is made choosing as reference values the duration of pressure variation in the chamber ($t_c = 1.0$ ms) and the initial chamber pressure value ($p_c = 1.286$ MPa). The resulting evolution in time of wall pressure is shown in Fig. 12, where the plots are relevant to times separated from each other by a constant time interval $\Delta t' = 0.3$. In all three cases the separation point, identified by the abrupt pressure increase in the extension, moves slowly at the beginning, then accelerates in the constant/positive gradient region. The case of COP nozzle also shows a deceleration of the separation point at the nozzle end.

The transition time, indicated as t'_{tr} in Table 2, can be defined as the time elapsed from the instant when the separation point leaves its initial location up to the instant when it reaches a new equilibrium position close to the nozzle lip. However, it is interesting to split

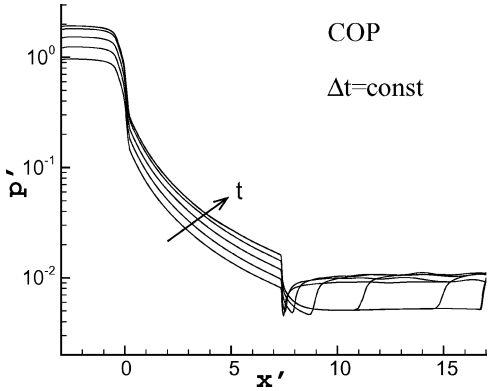

a) COP

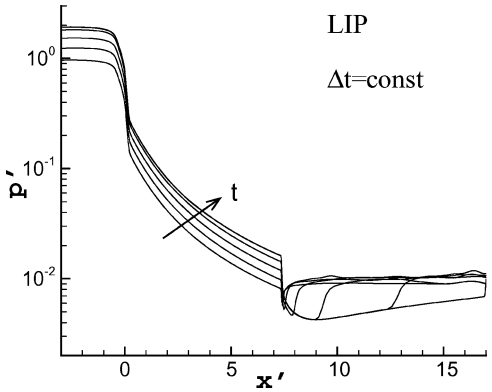

b) LIP

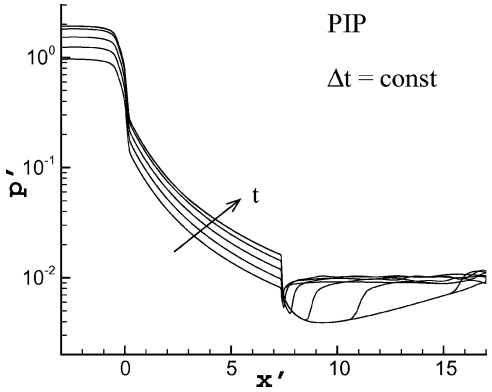

c) PIP

Fig. 12 Wall pressure plots at different times, separated each other by a constant time step, during transition.

the value of transition time t'_{tr} between the time $t'_{tr,1}$ the separation point spends moving from the initial location up to the location of minimum wall pressure in OM2 (see point C in Fig. 13), and the time $t'_{tr,2}$ spends migrating from the latter location to the final one. In particular, $t'_{tr,1}$ takes into account the evolution of the separation point in the region where wall pressure gradient is negative, namely, in the region where it can assume stable locations, depending on *PR*, like in conventional nozzles. The result is that $t'_{tr,1}$ increases from COP nozzle to LIP nozzle to PIP nozzle because of the increasingly stronger expansion at the inflection point. However, this value of time is mainly dependent on the variation of chamber pressure and represents the time interval where the nozzle flow behavior is still that of OM1, with the separation point located in the inflection point region (l'_i in Fig. 13).

The most important parameter characterizing the transition behavior is therefore the time $t'_{tr,2}$ during which the separation point location moves significantly, covering almost the whole extension of the dual-bell nozzle. As reported in Table 2, the larger the positive

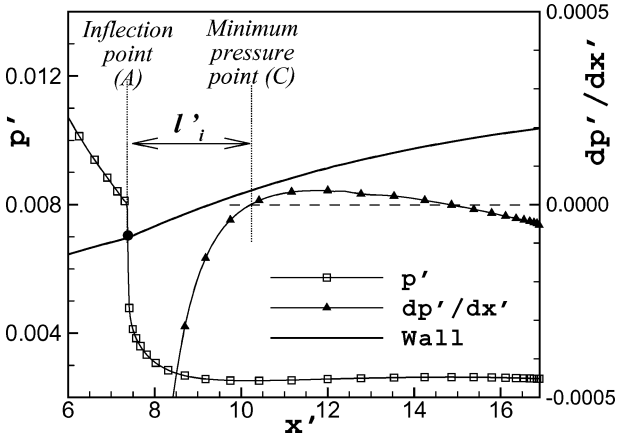

Fig. 13 Definition of the width of the inflection point region (l'_i).

gradient in the extension the shorter the interval of time $t'_{tr,2}$ spent by the separation point in the second bell. This is an important feature of positive gradient nozzles because as just mentioned the shorter the transition time, the shorter the interval of time during which side loads take place, and thus the lower the risk of structural failure. To complete the discussion of data reported on Table 2, it can be seen that the overall transition time t'_{tr} does not show a monotonic behavior from COP to PIP nozzles because of the opposite behavior of $t'_{tr,1}$ and $t'_{tr,2}$.

The behavior of wall pressures is also shown by the comparison made at the same time for all three nozzles in Fig. 14. In particular, at $t' = 1.2$ and 1.5 the separation point movement is delayed for LIP and PIP. Nevertheless, the acceleration of the separation point in case of positive values of pressure gradient is displayed by plots at $t' = 1.8$. At this instant the LIP nozzle displays a separation point location downstream that of the COP nozzle, whereas that of the PIP nozzle is still lagging behind. It should be remembered that chamber pressure doubles from $t' = 0$ to 1, and thus in all of the three instants shown in Fig. 14 the final chamber pressure has been already reached, whereas the effect of varying chamber pressure is delayed in the extension.

Finally, the steady-state evolution just discussed separately shows that the transition pressure ratio depends strongly on the pressure value reached at the end of the expansion at the inflection point region. For this reason, the stronger expansion that takes place in LIP and PIP nozzles moves the transition PR toward higher values. Indeed, as reported in the last column of Table 2, transition takes place at PR = 120 for PIP nozzle compared to the values of 102 and 110 for COP and LIP nozzles, respectively.

Scaling Effects

The analysis of different shapes of the extension has shown (see Figs. 5, 7, and 9) that, for increasing *PR*, during OM1 the separation point is not located exactly at the inflection point. On the contrary, it moves downstream of the inflection point, in a region where wall pressure gradient is negative. The width of this region, defined as l'_i in Fig. 13, can be important because, if wide enough, small asymmetric fluctuations of p_a or p_c can generate significant side loads. The width of the inflection point region obviously depends on the boundary-layer thickness ($l'_i = 0$ in the inviscid case), which in turn depends on the nozzle Reynolds number; therefore, its nondimensional value decreases for decreasing boundary-layer thickness (that is for increasing Reynolds number) and hence for increasing chamber pressure and/or nozzle dimension. To better understand the role of nozzle size and chamber pressure on l'_i and on the transition behavior, both steady-state and time-accurate simulations have been carried out considering different Reynolds numbers on the COP1 profile.

The steady-state solutions obtained increasing Reynolds number from $Re = 8.6 \times 10^6$ to $Re = 2.1 \times 10^9$ are displayed in Fig. 15, where an enlargement of the inflection point region is shown to

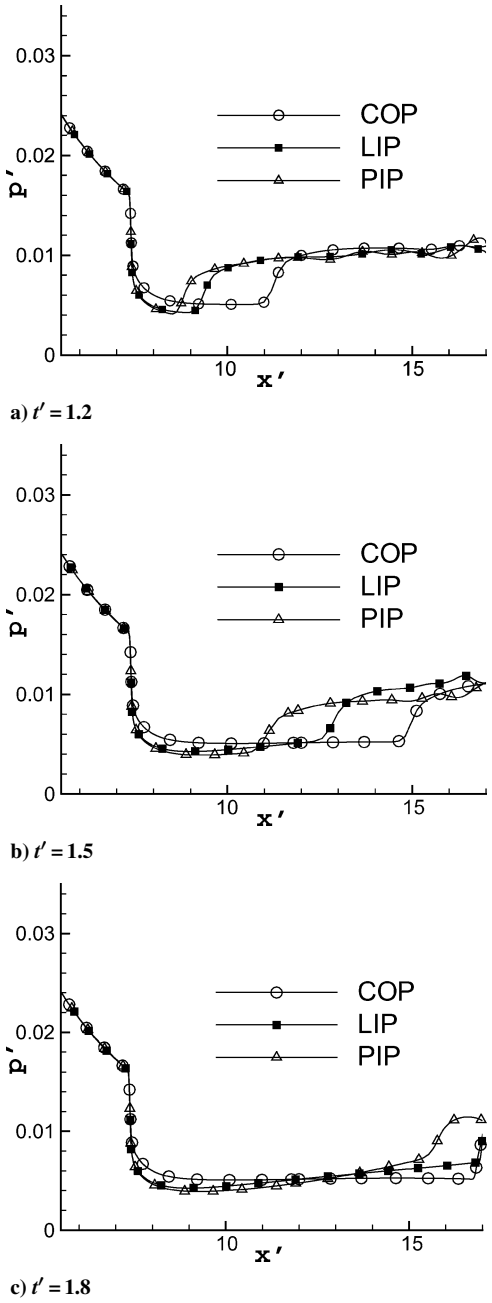

Fig. 14 Comparison of wall pressure behavior at selected times for the COP, LIP, and PIP nozzles.

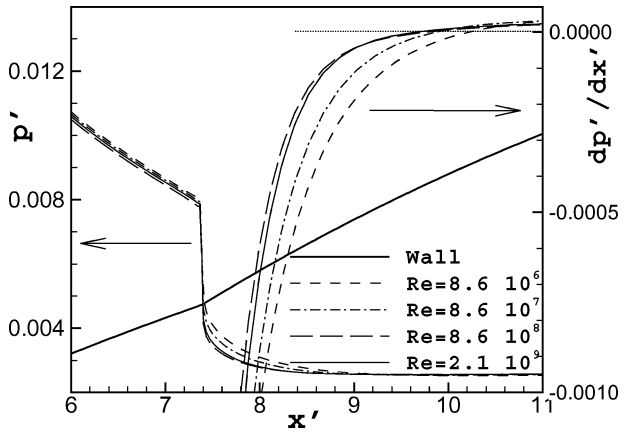

Fig. 15 Reynolds-number effect on expansion at the inflection point in case of attached-flow, wall pressure behavior, and derivative.

Table 3 Width of the inflection point region

Re	l'_i
8.6×10^6	2.86
8.6×10^7	2.49
8.6×10^8	2.41
2.1×10^9	2.29

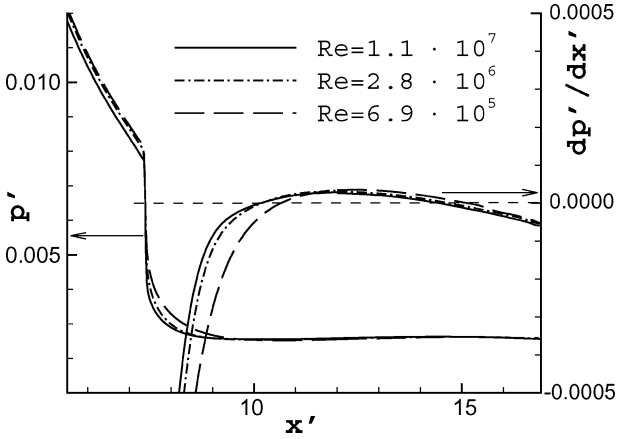

Fig. 16 Reynolds-number effect on wall pressure along the extension during OM2.

emphasize differences. The enlarged view shows that the inflection point region shrinks for increasing Reynolds number and also that its width is not negligible even in the case of the highest Reynolds number considered. In particular, Table 3 shows that for as high as $Re = 2.1 \times 10^9$, corresponding to the extreme case of a nozzle with a throat radius of 10 cm and a chamber pressure of 100 MPa with nitrogen gas and chamber temperature of 300 K, the inflection point region width can be of the same order of magnitude of the nozzle diameter. This is a not negligible feature especially considering that in the hot-gas cases for an assigned value of the product $p_c r_t$, Reynolds number is smaller than in the cold-gas case.

Once the width of the inflection point region has been recognized as significant, the just-mentioned possibility of having the separation point placed inside this region rather than exactly at the geometrical discontinuity must be considered thoroughly. Indeed, when pressure decreases along the nozzle wall the separation point will move toward the nozzle exit for decreasing ambient pressure and constant chamber pressure. The computations carried out for the present COP nozzle with $Re = 8.6 \times 10^6$ show that the separation point finds its equilibrium position in the inflection point region when *PR* is lower than 100 (Fig. 6). Because the nondimensional position of the separation point changes only slightly for varying Reynolds numbers, it can be inferred that in cases of 10% to 1% ambient pressure fluctuations, the subsequent tilt of the separation disk[7] will be 7 to 0.7 deg, respectively. As a consequence, possible asymmetric flow behavior in this region can yield side loads that should be carefully accounted for in the structural design of such a delicate zone of the nozzle.

A further aspect to be investigated is the effect of nozzle size on the duration of the transient. This study has been performed by considering three different time-accurate simulations featuring the same $t'_c = 1$, yet different Reynolds numbers. The value of the Reynolds number, computed at the beginning of the transient ($t' = 0$) increases from $Re = 6.9 \times 10^5$ to $Re = 1.1 \times 10^7$. The results are reported in Table 4, where, as discussed in the foregoing section, the most important parameter characterizing the transition behavior is the interval of time $t'_{\mathrm{tr},2}$, namely, the time spent by the separation point in the region of instability (the region with nearly zero or positive gradient in OM2). It can be noticed that $t'_{\mathrm{tr},2}$ remains nearly unchanged for increasing Reynolds number. This behavior is explained by the analysis of wall pressure gradient during OM2 (Fig. 16). In particular, the values of wall pressure gradient and the length covered by the

Table 4 Dependence of transition time on Reynolds number

Re	$t'_{\mathrm{tr},1}$	$t'_{\mathrm{tr},2}$	t'_{tr}
6.9×10^5	1.03	0.82	1.85
2.8×10^6	0.87	0.73	1.60
1.1×10^7	0.50	0.85	1.35

separation point do not change significantly from one value of one Reynolds number to the other. On the contrary, the values reported in Table 4 indicate that increasing Reynolds number reduces $t'_{\mathrm{tr},1}$. This is explained by the decreasing value of l'_i and by the increasing value of wall pressure gradient for increasing Reynolds number. Thus, the present analysis indicates that variations of the nozzle size play a more critical role in the evaluation of the possible insurgence of side loads during OM1 than in the evaluation of nozzle behavior during transition.

Conclusions

Three different dual-bell nozzles having a common first bell have been designed, and their performance in terms of thrust coefficient and behavior during the transition between the two main operating modes has been compared. The results indicate that the extension with constant wall pressure during high-altitude operation shows transition phase solutions characterized by the separation point steadily placed in a region that covers nearly one-fourth of the extension length. Profiles with positive pressure gradient show a better transitional behavior, with a sudden jump of the separation point from the inflection point region to nozzle exit. Nevertheless, if the pressure gradient is too small solutions with the separation point close to the nozzle end can still occur. Finally, the positive gradient shapes studied yield a rapid transition and display only a slight reduction of nozzle efficiency. The analysis of the effects of nozzle size has shown that a finite width of the inflection point region has to be expected also in the highest Reynolds-number range, and that increasing the Reynolds number yields a secondary effect on the transition time.

Acknowledgments

The present study is carried out in the framework of programs ESA/ESTEC-TRP, ESTEC Contract 15575/01/NL/CK, and ESA/ESTEC-GSTP, ESTEC Contract 16301/02/NL/SFc. Funding from the Italian Ministry of Scientific and Technological Research is also acknowledged. The authors thank the graduate student Luigi Arione who made some of the computations presented here during his thesis.

References

[1]Muss, J. A., Nguyen, T. V., Reske, E. J., and McDaniels, D. M., "Evaluation of Altitude Compensating Nozzle Concepts for RLV," AIAA Paper 97-3222, July 1997.

[2]Hagemann, G., Immich, H., Nguyen, T. V., and Dumnov, G. E., "Advanced Rocket Nozzles," *Journal of Propulsion and Power*, Vol. 14, No. 5, 1998, pp. 620–634.

[3]Horn, M., and Fisher, S., "Dual-Bell Altitude Compensating Nozzle," NASA CR-194719, 1994.

[4]Goel, P., and Jensen, R. J., "Numerical Analysis of the Performance of Altitude Compensating Dual Bell Nozzle Flows," *Proceedings of the 32nd JANNAF Combustion Subcommittee Meeting and Propulsion Engineering Research Center 7th Annual Symposium*, Vol. 2, CPIA, Columbia, MD, 1995, pp. 117–140.

[5]Hagemann, G., Frey, M., and Manski, D., "A Critical Assessment of Dual-Bell Nozzles," AIAA Paper 97-3299, July 1997.

[6]Hagemann, G., Terhardt, M., Haeseler, D., and Frey, M., "Experimental and Analytical Design Verification of the Dual-Bell Concept," *Journal of Propulsion and Power*, Vol. 18, No. 1, 2002, pp. 116–122.

[7]Schmucker, R. H., "Flow Process in Overexpanded Chemical Rocket Nozzles. Part 2: Side Loads due to Asymmetric Separation," NASA TM-77395, Feb. 1984.

[8]Dumnov, G. E., Ponomaryov, N. B., and Voinov, A. L., "Dual Bell Nozzles for Rocket Engines of Launch Veichle Upper Stages and Orbital Transfer Vehicles," AIAA Paper 97-3089, July 1997.

[9]Nasuti, F., Onofri, M., and Martelli, E., "Numerical Study of Transition between the Two Operating Modes of Dual-Bell Nozzles," AIAA Paper 2002-3989, July 2002.

[10]Ahlberg, J. H., Hamilton, S., Migdal, D., and Nilson, E. N., "Truncated Perfect Nozzles in Optimum Nozzle Design," *ARS Journal*, Vol. 31, No. 5, 1961, pp. 614–620.

[11]Rao, G. V. R., "Exhaust Nozzle Contour for Optimum Thrust," *Jet Propulsion*, Vol. 28, No. 6, 1958, pp. 377–382.

[12]Rao, G. V. R., "Approximation of Optimum Thrust Nozzle Contour," *ARS Journal*, Vol. 30, No. 6, 1960, p. 561.

[13]Nasuti, F., and Onofri, M., "Analysis of Unsteady Supersonic Viscous Flows by a Shock Fitting Technique," *AIAA Journal*, Vol. 34, No. 7, 1996, pp. 1428–1434; also AIAA Paper 95-2159, July 1995.

[14]Nasuti, F., "A Multi-Block Shock-Fitting Technique to Solve Steady and Unsteady Compressible Flows," *Computational Fluid Dynamics 2002*, edited by S. Armfield, P. Morgan, and K. Srinivas, Springer-Verlag Berlin, 2003, pp. 217–222.

[15]Nasuti, F., and Onofri, M., "Flow Analysis and Methods of Design for Dual-Bell Nozzles," AIAA Paper 2001-3558, July 2001.

[16]Nasuti, F., Onofri, M., and Martelli, E., "Analysis of the Transition Process in Dual-Bell Nozzles," *Proceedings of the 4th International Conference on Launcher Technology*, CD-ROM, CNES, Toulouse, France, 2002.

[17]Paciorri, R., and Sabetta, F., "Compressibility Correction for the Spalart-Allmaras Model in Free-Shear Flows," *Journal of Spacecraft and Rockets*, Vol. 40, No. 3, 2003, pp. 326–331.

[18]Spalart, P. R., and Allmaras, S. R., "A One-Equation Turbulence Model for Aerodynamic Flows," *La Recherche Aerospatiale*, No. 1, 1994, pp. 5–21.